Impact of 440 GeV Proton beams on Superconductors in a Cryogenic Environment

A. Will[1,2]**, A. Bernhard**[2]**, M. Bonura**[3]**, B. Bordini**[1]**, M. Mentink**[1]**, A.-S. Mueller**[2]**, A. Oslandsbotn**[1]**, R. Schmidt**[1]**, J. Schubert**[1]**, C. Senatore**[1,3]**, A. Siemko**[1]**, A. Verweij**[1] **and D. Wollmann**[1]

[1] CERN, Geneva, Switzerland
[2] Karlsruhe Institute of Technology (KIT), Karlsruhe, Germany
[3] University of Geneva, Switzerland

E-mail: `andreas.will@cern.ch`

Abstract. The superconducting magnets used in high energy particle accelerators such as CERN's LHC can be impacted by the circulating beam in case of specific failures. This leads to interaction of the beam particles with the magnet components, like the superconducting coils, through direct beam impact or via secondary particle showers. The interaction causes energy deposition in the timescale of microseconds and induces large thermal gradients within the superconductors, which are in the order of 100 K/mm. To investigate the effect on the superconductors, an experiment at CERN's HiRadMat facility was designed and executed, exposing short samples of Nb-Ti and Nb$_3$Sn strands in a cryogenic environment to microsecond 440 GeV proton beams. The irradiated samples were extracted and analyzed for their critical transport current I_c. This paper describes the results and analysis of the measurements of I_c as well as thermo-mechanical simulations of the Nb$_3$Sn strands to evaluate the degradation of I_c as a function of the mechanical strain present during and after the beam impact.

1. Introduction

In order to understand the damage limits of superconducting accelerator magnets due to direct beam impact, an experiment was performed in 2018 at CERN's HiRadMat facility [1]. In this experiment, short samples of superconducting Nb$_3$Sn and Nb-Ti strands were impacted by 440 GeV proton bunches, while being in a cryogenic environment close to 4 K. The samples were made of LHC dipole type Nb-Ti strand with a diameter of 0.825 mm [2] and HL-LHC inner triplet Nb$_3$Sn RRP© 108/127 strand with a diameter of 0.85 mm, respectively [3]. The length of the samples was 50 mm. The samples were embedded in a copper sample holder and arranged in batches of ten along the beam axis. The energy deposition varies as a function of their longitudinal placement. One beam pulse was applied per batch of strands, the hot spot temperatures for the strands within one batch varied from 290 K to 1200 K. The energy deposition in the copper sample holder was calculated with FLUKA [4, 5] as a function of the parameters of the impacting beam. The temperature in the samples was scaled using the heat capacity of copper. Both calculations are shown in Fig. 1. The beam size was fixed to 1.1 mm σ and the pulse consisted of 24 bunches with a total charge of 3.1×10^{12} protons/pulse and a pulse duration of 0.6 µs. Due to the small beam size, the energy deposition and the temperature profile show large gradients within the strands, in the order of ~100 K/mm. A detailed description of
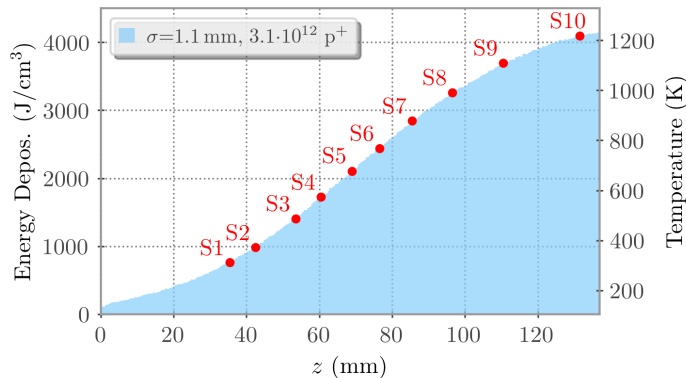
Figure 1. Peak energy deposition in the sample holder along the beam axis, calculated with FLUKA [4, 5]. The corresponding peak temperatures reached in copper are indicated on the right axis. The red dots indicate the position of the Nb-Ti and Nb_3Sn strand samples.

the experimental setup and the visual inspection of the strands after the beam impact experiment was given in [6]. This paper describes the results of the following analysis of the critical transport current I_c, of both Nb_3Sn and Nb-Ti as well as RRR measurements of the Nb-Ti strands. Furthermore, a coupled multi-physics simulation was performed to evaluate strain levels during and after the beam impact. The strain distribution is used as input for microscopic strain dependent models for the critical transport current density in Nb_3Sn, in order to correlate the measured and simulated degradation of the critical transport current of the full strand.

2. Nb-Ti strands
Two batches of ten Nb-Ti strands have been used in this experiment. This section describes the post-irradiation analysis, consisting of critical transport current and RRR measurements.

2.1. Critical transport current measurements
The critical transport current of the first batch of Nb-Ti samples has been measured after their extraction from the experiment, and the results are shown in Fig. 2. No significant reduction in critical transport current was observed in any of the examined samples. This is coherent with previous beam impact experiments on Nb-Ti strands at room temperature [7], where the critical current density was derived from magnetization measurements. However, all measured strands showed a reduction in thermal stability at low fields, i.e. with larger transport currents. The critical current for samples S5 and S6 could only be determined at 5 T and above, sample S7 from 6 T and sample S8 from 8 T. For samples S9 and S10 the critical current could only be measured at 9 T. When removing the samples from the critical current measurement setup, samples S5 and S6 broke at the beam impacted area. The observed thermal instability is assumed to result from a weakening in the copper matrix due to the thermo-mechanical stresses during the beam impact.

2.2. RRR measurements
To confirm changes in the copper matrix, RRR measurements were performed on all intact samples besides S5 and S6. The results showed a reduction of RRR with increasing energy deposition. RRR decreased from around 220 for the reference sample to 155 for sample S9 and 185 for S10 as shown in the data points for the full strands of Fig. 3. The plotted values were obtained by measuring the strand resistance over the full sample length. As it is assumed that the resistance only increased close to the beam impact, the peak of the RRR degradation was estimated, using a gaussian resistivity profile, similar to the beam profile (see plot for minimum RRR in Fig. 3). The error bars assume a 2% error on the resistivity measurements and a 50% uncertainty of the width of the damaged region. The minimum quench energy (MQE) is
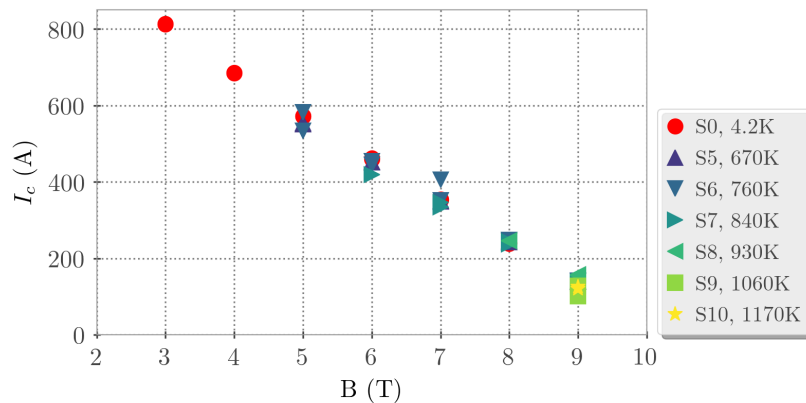
Figure 2. Measured critical transport current I_c, for S5 to S10 and the reference sample S0.

proportional to RRR, therefore, the reduction of MQE in the strand can be directly derived from the RRR reduction at the beam impacted zone. The remaining fraction of MQE is indicated on the right axis of Fig. 3. For samples S7 to S10, MQE is reduced to 20% of the reference value and below. This can explain the observed thermal instabilities of the samples.
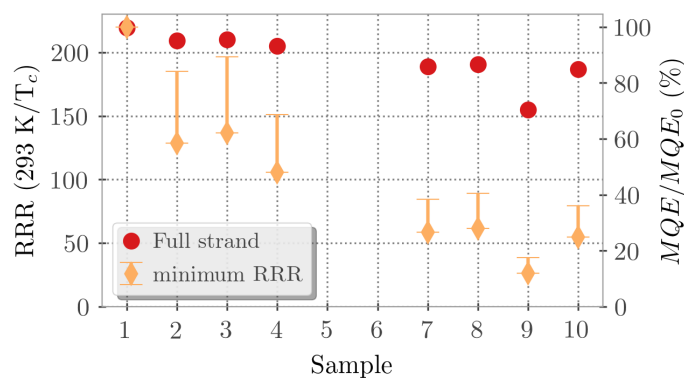

Figure 3. Measured RRR between room temperature and the critical temperature T_c of the Nb-Ti strands, and derived minimum RRR values at the beam impact. The right axis shows the remaining fraction of the minimal quench energy.

3. Nb$_3$Sn strands

A total of three batches of 10 samples of Nb$_3$Sn strands each were used in this experiment. The strands were heat treated in quartz tubes to assure perfect sample straightness, with dwells at 210 °C, 400 °C and a final reaction temperature of 665 °C. They were then cut to 50 mm pieces and mounted in the sample holder.

3.1. Microscopic model for strain dependent critical current density

The general scaling for the critical current density J_c as a function of the self-field corrected magnetic flux density B, the temperature T and strain ε of Nb$_3$Sn filamentary strands is,

$$J_c(B, T, \varepsilon) = C_1 (1 - t^2) \, b^{-0.5} \, (1 - b)^2, \tag{1}$$

$$t = \frac{T}{T_c \cdot s(\varepsilon)^{\frac{1}{3}}}, \tag{2}$$

$$b = \frac{B}{B_{c2}(T, \varepsilon)}, \tag{3}$$

$$B_{c2}(T, \varepsilon) = B_{c2,0} \cdot s(\varepsilon) \cdot (1 - t^{1.5}), \tag{4}$$
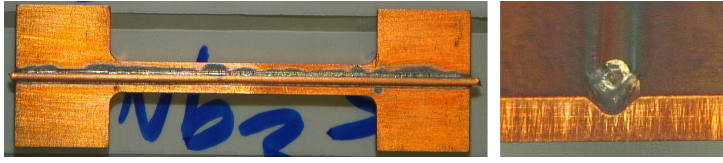
Figure 4. Grooved copper support, for mechanical and thermal stabilization of the Nb$_3$Sn samples during the I_c measurements. The samples were soldered onto the support.
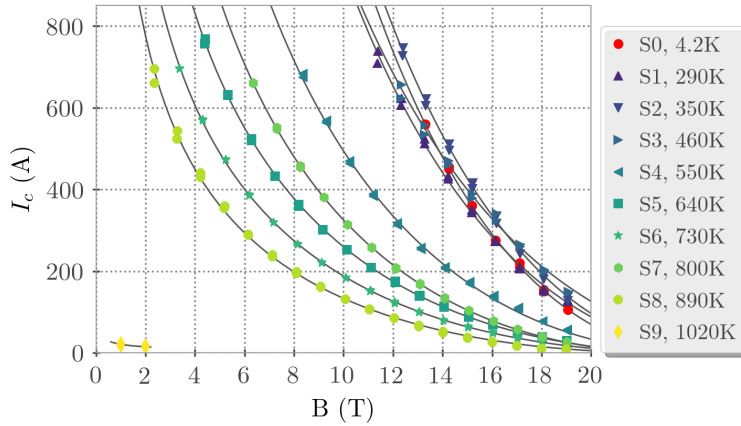

Figure 5. Measured critical transport current for S1-S9 and the reference sample S0. Sample S10 was completely damaged and is omitted. The gray lines are fits in the form of Eq.(1).

where $B_{c2,0}$ is the upper critical field at zero strain and zero temperature, T_c the critical temperature and $s(\varepsilon)$ the strain dependent function [8]. C_1 is a fit parameter, t the reduced temperature and b the reduced field. This has been shown to be accurate for a large scale of Nb$_3$Sn conductors and allows to separate the strain dependence from the other conductor properties such as T_c and $B_{c2,0}$ [9]. In this paper T_c=16.8 K and $B_{c2,0}$=29.5 T are fixed as reference values of the non-degraded strands.

There are several proposals for $s(\varepsilon)$ published in literature. The presented work relies on Ekin's power law model

$$s(\varepsilon) = 1 - a_{\pm} \left| \varepsilon + \varepsilon_{max} \right|^u \tag{5}$$

with $u = 1.7$, $a_+ = 1250$ and $a_- = 900$ as fitted for the HL-LHC strand type[10]. a_- describes the compressive and a_+ the tensile strain. $\varepsilon_{max} \sim -0.001$ originates from the difference in thermal contraction between the copper matrix and the Nb$_3$Sn filaments when cooled down to 4.2 K [11].

3.2. Critical current measurements and analysis

The measurement setup allows a maximum transport current of ∼800 A and magnetic fields up to 19 T to be applied to the samples. The critical transport current was measured at 4.2 K. Due to the short sample length of 50 mm it was necessary to solder the samples on copper supports shown in Fig. 4. These allowed for mechanical and thermal stabilization.

The critical transport current of the first batch of Nb$_3$Sn samples was measured and is shown in Fig. 5. The results are self field corrected, assuming the long straight wire approximation [12]. Samples S1 to S3 showed small variations but no significant degradation of the critical current with respect to the reference sample S0. Sample S5 to S8 show progressive reduction in the critical transport current, with exception of S7, which lies in between S5 and S6. Sample S9 showed negligible and S10 no critical current at all.
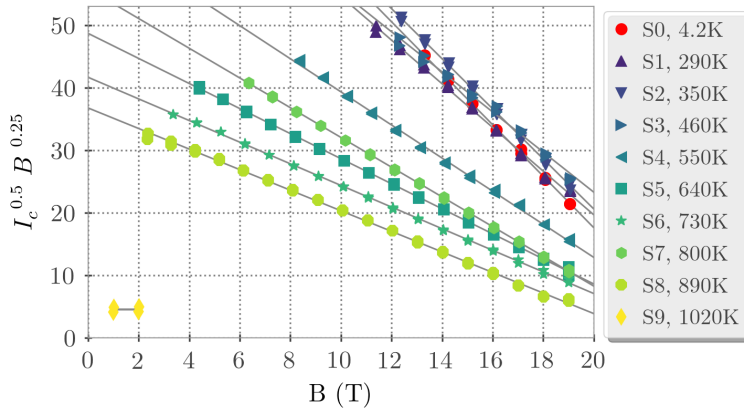
Figure 6. Kramer representation of the critical current measurements according to Eq.(6). The gray lines are fits with a linear function to obtain B_{c2}.
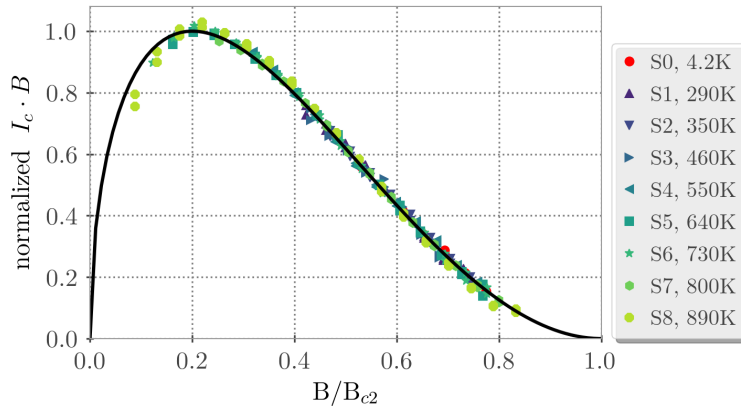

Figure 7. Normalized pinning force over reduced field $b=B/B_{c2}$. All curves were normalized with respect to the maximum of the according sample curve. b was calculated using B_{c2} from the fit of each sample. S9 was omitted due to a lack of measurement data.

A fit in form of Eq. 1 has been applied, where $\frac{T}{T_c} = \frac{4.2\ K}{16.8\ K}$ was fixed and the constants C_1 and $B_{c2}(\varepsilon)$ were fitted for each of the samples. The fits are shown in Fig. 5 as gray lines. The results for the fitted B_{c2} are shown in Fig. 8 and will be discussed below.

The Kramer representation

$$f_k = I_c^{0.5}\ B^{0.25} \quad \propto \quad C_k \cdot (B_{c2} - B) \tag{6}$$

is used to determine $B_{c,2}(4.2\ \mathrm{K})$ from the critical transport current measurements. The Kramer form and the resulting linear fits are shown in Fig. 6. The corresponding fit results for $C_k \propto \sqrt{C_1}$ and $B_{c,2}(4.2\ \mathrm{K})$ are shown in Fig. 8.

The absolute pinning force

$$F_p = I_c \cdot B \tag{7}$$

was calculated for each sample. Figure 7 shows the normalized values with respect to the maximum pinning force of each sample, plotted over the reduced field $b=B/B_{c2}$, where B_{c2} was derived from fitting F_p to the measured data. A fundamental change in the pinning mechanism was not observed. The maximum of the pinning force reduces, but the relative position stays constant at b∼0.2. The reduction of the maximum is probably due to filament breaking, leading to a reduction of active superconductor cross section.
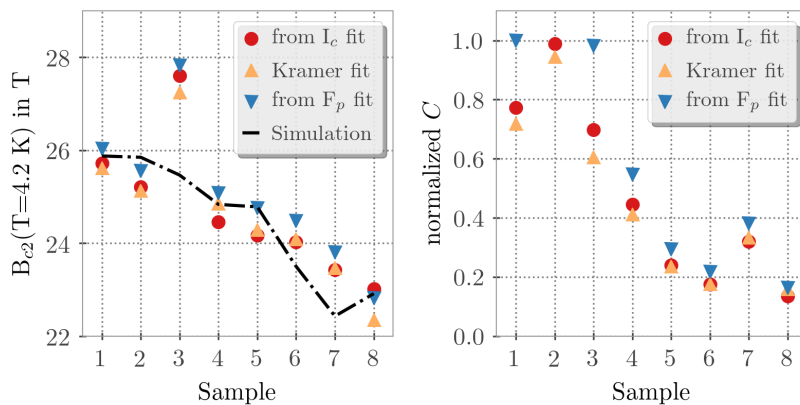
Figure 8. Fit-results for the constants C and B_{c2} from the three different fits, critical current scaling in Eq.(1) - red dots -, Kramer representation in Eq.(6) - orange triangles - and the pinning force in Eq.(7) - blue triangles. The values for C are normalized with respect to the reference sample.

3.3. Discussion of Fit-Results

Three different models have been fitted to the measured data. The critical current Eq.(1), Kramer form Eq.(6) and the pinning force Eq.(7). The comparison of the fit results for the scaling constants C and the upper critical field B_{c2} are shown in Fig. 8. All models yield consistent results. While the Kramer form is numerically the most stable to determine B_{c2}, the pinning force fit yields a stable measure for the scaling constant C.

The visible reduction of B_{c2} can be explained via the strain dependent model Eq.(4) and suggests a degradation due to residual strain, e.g. due to deformation of the copper matrix, that imposes strain onto the Nb$_3$Sn filaments. The rather modest degradation of B_{c2} cannot solely explain the degradation of I_c according to Eq.(1). On the other hand, the scaling constant C is associated with the general reduction of critical current, independent of the magnetic field B. A reduction of this value can most likely be explained by individual filaments cracking and/or breaking when exceeding the irreversible strain limit [13, 14]. These filaments can no longer contribute to the current transport, therefore reducing only C with no influence on B_{c2}. The relative reduction of C, as shown on the right hand side of Fig. 8, is therefore related to the amount of filaments being broken or not contributing significantly anymore due to large strain. The reduction of B_{c2} originates from the intact filaments, that are degraded due to residual strain of the embedding copper matrix.

3.4. Transient thermo-mechanical simulations with FLUKA and ANSYS

Transient thermo-mechanical simulations were performed to study the origin of the degradation of I_c and B_{c2} in the strand samples. At first, the thermal behaviour in the strands during and after the beam impact was calculated in ANSYS, using the energy deposition previously calculated with FLUKA[4, 5] and scaling it to a heating rate via the pulse length of the beam impact of 0.6 μs. The transient mechanical behaviour of the strands was subsequently simulated with ANSYS. A mechanical solver calculated the evolution of the mechanical deformation of the strands and the sample holder as well as the residual strain after the beam impact. Material properties were used from literature where available and from internal material databases or measurements [16, 17, 18, 19, 20, 21, 22, 23].

A simplified strand geometry was used, where the Nb$_3$Sn phase is modelled as a cylindrical shell, as a mixture of Nb$_3$Sn and the copper matrix. The cylinder shell covers the filament region. The material properties of this shell were chosen to represent the local copper to superconductor ratio. Furthermore, material properties from tensile tests were used, which show a semi-plastic behavior for the Nb$_3$Sn phase [16]. The plastic strain within the cylinder shell of the mixed material was evaluated.
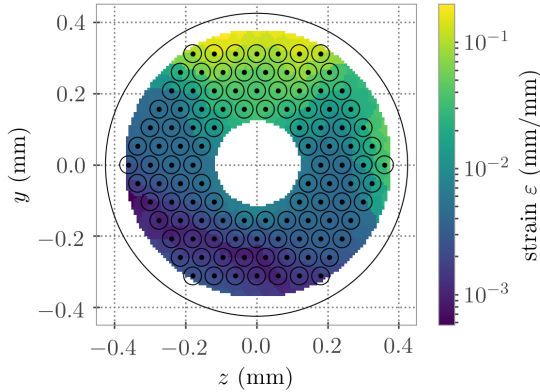
Figure 9. Simulated residual plastic strain in the composite material region. As a reference, the filament positions as well as the outer strand radius are indicated by black circles.

The sample holder was included in the simulations and modelled as laminated block of copper with cut outs for the strand samples. A detailed description of the experimental setup can be found in [6]. The visual inspection during the extraction of the samples revealed imprint marks from the sample holder and kinks around the beam impact region [6]. The simulation confirmed a significant influence of the sample holder on the plastic deformation of the strand's copper matrix, originating from the thermal expansion of the sample holder into the grooves and therefore onto the samples. It is important to mention, that the heat treated copper, contained in the Nb_3Sn strands is significantly softer than the cold worked copper of the sample holder. The simulation showed the squeezing of the samples starting from sample S4 and higher. Furthermore, the simulations suggest, that the kinks in the strands originate from oscillations of the strand due to the large thermal gradients and the resulting imbalance in thermal expansion after the beam impact.

3.5. Application of microscopic models to calculate I_c degradation

The critical transport current of an impacted strand was calculated based on the simulated strain distribution. A combination of J_c degradation according to Eq.(1) and degradation via filament fracturing when crossing an irreversible strain limit ε_{irr} was assumed. Scaling according to Eq.(1) takes into account the residual absolute strain in the mixed material area. For the filament fracturing, the criterion is the maximum value of the longitudinal strain during the beam impact event.

Only the cross section in the beam impact center is considered. It shows the maximum strain distribution and, therefore, the highest degradation, acting as the bottle neck in the critical transport current measurement. Figure 9 shows the simulated absolute residual strain for sample S5. The inhomogeneous distribution of the strain over the strand cross-section is caused by a 1 mm vertical offset of the beam during the experiment [6].

$s(\varepsilon)$, B_{c2} and J_c are calculated from the results of the finite element simulations at each mesh-node in the mixed material region, using Eqs. (5), (4) and (1). Figure 10 shows the distribution of B_{c2} and J_c in the cross section of sample S5 with highest degradation. The gradient in strain results accordingly to a gradient in B_{c2}. As visible in the left plot of Fig. 10, regions of non-degraded B_{c2} remain. These regions dominate the resulting I_c of the strand. Filaments within the red marked areas in the right plot of Fig. 10 are assumed to be fractured and no longer contribute to I_c.

I_c is hereby calculated as the surface-integral of the J_c distribution in the mixed material region. Fig. 11 compares the simulated and measured I_c of sample S5 as a function of the magnetic flux density. The dashed orange line shows the simulated I_c due to the effect of residual strain (see Eq.(1)). The B_{c2} derived from the Kramer fit for this result is in good
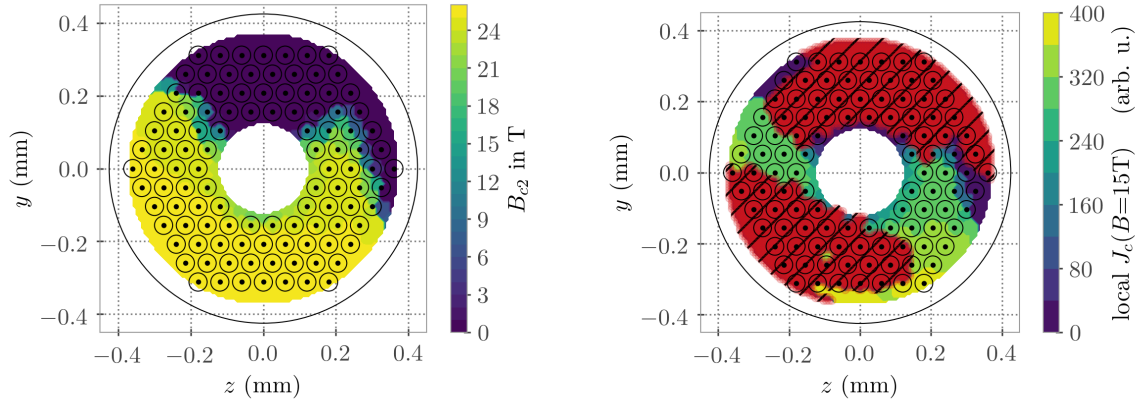
Figure 10. *Left:* Calculated upper critical field B_{c2} based on the simulated strain map and microscopic model Eq.(4). *Right:* Calculated critical current density J_c at 15 T, based on the simulated strain map using the scaling in Eq.(1). The filaments in the red marked areas are assumed to be broken, having experienced a longitudinal strain of $\varepsilon \geq \varepsilon_{irr} = 0.262$ %, therefore no longer contributing to the cross section integral.
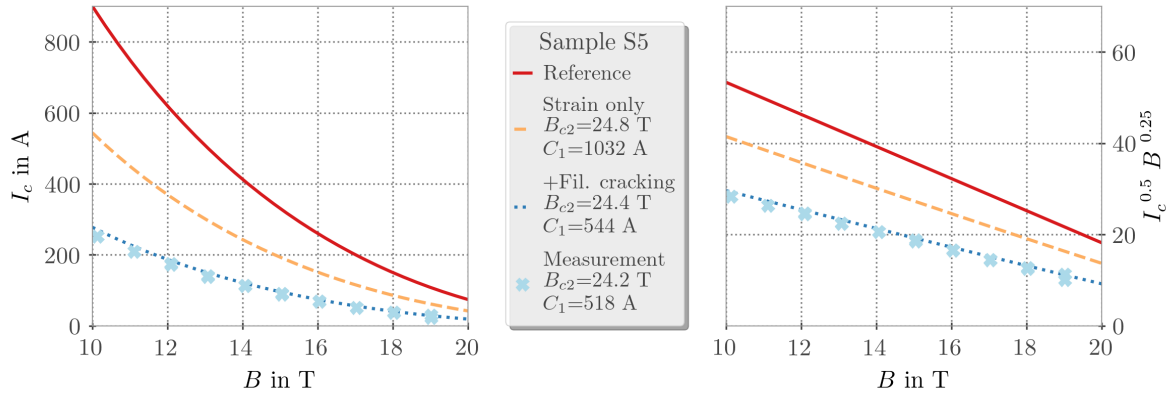

Figure 11. *Left:* Comparison of simulated and measured I_c of sample S5 as a function of the magnetic flux density based on the simulated strain distribution and the microscopic strain model Eq.(1). The fit parameters from a fit of form Eq.(1) are indicated. *Right:* Kramer form of the simulated and measured I_c data.

agreement with the measurements. The absolute I_c however is not well reproduced. The blue dotted line includes in addition filament fracturing by introducing an irreversible strain limit ε_{irr}. Regions with strain values above ε_{irr} are not considered for the calculation of I_c.

The real irreversible strain limit of a Nb_3Sn strand depends on factors like the heat treatment or the material composition, and, therefore, varies for each specific conductor type [13, 14]. Furthermore, it is rather a region of strain, where fracturing occurs, with a steep beginning at a certain "irreversible strain cliff" $\varepsilon_{irr,0}$ [14]. Literature values for $\varepsilon_{irr,0}$ of the RRP conductor usually vary in the range from 0.1 to 0.4 %, but mostly lie around 0.3 % [14, 15]. For sample S5 the best fit between measured and calculated I_c curve (see Fig. 11) was found for $\varepsilon_{irr} = 0.262$ %, which is in good agreement with the above quoted literature values.

The simulations, described above for sample S5, were performed for all samples. Good fits

between measured and simulated I_c curves could be found, fitting the values of ε_{irr} for each case. All values were within $\varepsilon_{irr} = 0.35 \pm 0.1$ % and, therefore, physically reasonable. The simulated B_{c2} values are shown in Fig. 8.

4. Summary and Conclusion

The thermal stability of the Nb-Ti strands was largely reduced after being exposed to beam. Therefore, with increasing hot spot temperature the critical currents could only be measured at increasing external fields. However, the measured critical currents were not found to be degraded. This behaviour could be explained by a reduction of the minimum quench energy, which was supported by an observed reduction of the local RRR in the beam impact regions. This can have an impact on the operability of an accelerator magnet regarding its thermal stability.

Irradiated Nb$_3$Sn samples have been measured for their critical transport current I_c. The analysis using fits of the Kramer form as well as the general scaling law for filamentary Nb$_3$Sn conductors revealed a modest degradation of B_{c2} and a strong degradation of the absolute value of I_c with increasing hot spot temperature. Samples with hot spot temperatures below ~ 460 K showed no significant decrease in critical current. All irradiated samples, except S1, showed a decrease in B_{c2}. After the impact, B_{c2} ranges from ~ 26 T to below ~ 23 T in the worst case of sample S8. The two samples with the highest hot spot temperatures (S9 and S10) were destroyed by the beam impact and could not carry any current in the superconducting phase.

Transient thermo-mechanical simulations were performed to understand the critical current degradation due to the beam impact. Using strain dependent scaling laws, the decrease in B_{c2} could be explained via the residual strain in the Nb$_3$Sn phase. This is most likely due to a deformation of the surrounding copper matrix. It could be shown that the absolute measured degradation of I_c is dominated by damaging a large fraction of filaments, when reaching the irreversible strain limit ε_{irr}. Taking ε_{irr} as a free fit parameter, the model derived physically reasonable ε_{irr} values. A good agreement between simulated and measured critical transport currents was observed. However, given the variability and uncertainty of the irreversible strain limits and the sensitivity of the model to this parameter, an accurate prediction of I_c degradation remains challenging, while for B_{c2} the model seems rather robust.

Therefore, experiments remain important to determine the damage limits of superconducting magnets and to validate simulation results.

Acknowledgments

References

[1] Efthymiopoulos I *et al.* 2011 *Proc. 2nd Int. Particle Accelerator Conf. IPAC'11* (San Sebastian), paper TUPS058
[2] Boutboul T, Le Naour S, Leroy D, Oberli L and Previtali V 2006 *IEEE Transactions on Applied Superconductivity*, vol. **16**-2
[3] Ferracin P *et al.* 2014 *IEEE Transactions on Applied Superconductivity*, vol. **24**-3
[4] Boehlen T T, Cerutti F, Chin M P W, Fasso A, Ferrari A, Ortega P G, Mairani A, Sala P R, Smirnov G and Vlachoudis V 2014 *Nuclear Data Sheets* **120**, 211-214, URL: http://www.fluka.org
[5] Ferrari A, Sala P R, Fasso A, and Ranft J 2005 *CERN-2005-10, INFN/TC_05/11, SLAC-R-773*
[6] Will A *et al.* 2019 *Proc. 10th Int. Particle Accelerator Conf. (IPAC'19)*, Melbourne, Australia
[7] Raginel V *et al.* 2018 *IEEE Transactions on Applied Superconductivity*, vol. **28**-4
[8] Mentink M G T, *Critical surface paramterization of a high Jc RRP Nb3Sn strand* 2008 *Internship report*, Lawrence Berkeley National Laboratory

[9] Mentink M G T 2014 *An experimental and computational study of strain sensitivity in superconducting Nb3Sn*, (Enschede: University of Twente)

[10] Ekin J W, Cheggour N, Goodrich L, Splett L, Bordini B and Richter R 2016 *Supercond. Sci. Technol.* **29** 123002 (38pp)

[11] Bordini B, Alknes P, Bottura L, Rossi L and Valentinis D 2012 *Supercond. Sci. Technol.* **26** 075014 (10pp)

[12] Godeke A, Chlachidze G, Dietderich D R, Ghosh A K, Marchevsky M, Mentink M G T and Sabbi G L 2013 *Supercond. Sci. Technol.* **26** 095015 (15pp)

[13] Jewell M C 2008 *The Effect of Strand Architecture on the Fracture Propensity of Nb3Sn Wires* (Madison, WI: UMI Dissertation Publishing)

[14] Cheggour N, Stauffer T C, Starch W, Goodrich L F and Splett L D 2019 *Scientific Reports* **9** 5466

[15] Cheggour N, Stauffer T C, Starch W, Lee P J, Splett J D, Goodrich L F and Ghosh A K 2018 *Scientific Reports* Vol **8** 13048

[16] Ferradas J 2018 Electromechanical characterization of Nb3Sn conductors at University of Geneva, *Workshop on Nb3Sn technology for accelereator magnets* (Paris), contribution 3154561

[17] Davies A 2011 Material properties data for heat transfer modeling in Nb_3Sn magnets, Internship Report Ilinois Acceleration Institute

[18] Li Y and Gao Y 2017 GLAG theory for superconducting property variations with A15 composition in Nb_3Sn wires, Scientific Reports Vol. **7** 1133

[19] Mitchel N 2005 Finite element simulations of elasto-plastic processes in Nb_3Sn strands, Cryogenics **45**(7):501-515

[20] Scheuerlein C, Fedelich B, Alkens P, Arnau G, Bjoerstad R and Bordini B 2015 IEEE Trans. Appl. Supercond. **25**-3 8400605

[21] Wang K and Reeber R R 1996 Thermal Expansion of Copper, High Temperature and Materials Science vol. **35**

[22] Simon N G and Reed R P 1987 Cryogenics properties of copper and copper alloy, (Washington) NIST Monograph **177**

[23] Przybyszewski J S 1968 Stress-Strain Behavior of Cold-Welded Copper-Copper Microjunctions in Vacuum as determined from electrical Resistance Measurements, NASA Technical Note D-4743